ADVANCED FUNCTIONAL MATERIALS
www.afm-journal.de

Exploiting the Functionality of Cerium Oxide-Modified Carbon Nanohorns Catalysts Toward Enhanced CO_2 Reduction Performance

Alessia Pollice, Michele Cacioppo, Miriam Marchi, Miriam Moro, Francesco Paolucci, Marcella Bonchio, Maurizio Prato, Giovanni Valenti, Michele Melchionna,* and Paolo Fornasiero*

The suitable interfacial combination of CeO_2 and oxidized carbon nanohorns (CeO_2@oxCNHs) is instrumental to the control of the activity and selectivity in CO_2 reduction reaction (CO_2RR). This study presents a newly developed synthetic approach that integrates the CeO_2 and CNH to form extended interfacial domains, resulting in a higher performance for CO_2RR as compared with previously reported ceria-nanocarbon catalysts. In particular, detailed electrochemical characterization reveals that the CeO_2@oxCNHs nanocomposite synthesized with this newly developed solvothermal method exhibits up to ten times higher current density (*j*) than its counterpart prepared by conventional sol-gel method and can be effectively integrated into a state-of-the-art gas diffusion electrode (GDE) device. The combination of high-surface area oxCNH with the gas diffusion electrode configuration boosts the CeO_2 efficiency in converting CO_2 to products involving C—C couplings as ethanol and acetaldehyde, even at very low overpotentials, offering a promising pathway for developing nanocomposite materials for CO_2 reduction.

1. Introduction

Electrocatalytic reactions offer a safe and environmentally friendly way to convert chemical energy into electrical energy and vice versa.[1] The carbon dioxide reduction reaction (CO_2RR) represents a key technology in the energy sector, as it converts electrical energy into stored chemical energy in the form of e-fuels. However, while in the case of electrocatalytic hydrogen evolution reaction (HER) the mechanism is well-understood, the CO_2RR remains a significant challenge due to the complexity of its reaction pathways, leading to a wide range of products.[2,3] The CO_2 conversion is influenced by factors such as pH, solvation, and most importantly, reactor design and the catalyst's structure. A severe limitation for CO_2RR large-scale exploitation is the low CO_2 solubility threshold

A. Pollice, M. Moro, F. Paolucci, G. Valenti
Department of Chemistry "Giacomo Ciamician"
Alma Mater Studiorum – Università di Bologna
Via Piero Gobetti 85, Bologna 40129, Italy
E-mail: g.valenti@unibo.it

A. Pollice, F. Paolucci, G. Valenti
Center for Chemical Catalysis "C3"
Alma Mater Studiorum – Università di Bologna
Via Piero Gobetti 85, Bologna 40129, Italy

The ORCID identification number(s) for the author(s) of this article can be found under https://doi.org/10.1002/adfm.202509299

[+]Present address: Department of Biological, Chemical and Pharmaceutical Sciences and Technologies (STEBICEF),University of Palermo, Viale delle Scienze, Edificio 17, Palermo 90128, Italy

DOI: 10.1002/adfm.202509299

M. Cacioppo[+], M. Prato
Center for Cooperative Research in Biomaterials (CIC biomaGUNE)
Basque Research and Technology Alliance (BRTA)
Paseo Miramón, 194, Donostia San Sebastián 20014, Spain

M. Marchi, M. Prato, M. Melchionna, P. Fornasiero
Department of Chemical and Pharmaceutical Sciences, INSTM UdR Trieste
University of Trieste
Via Licio Giorgieri, 1, Trieste 34127, Italy
E-mail: melchionnam@units.it

F. Paolucci
Institute of Condensed Matter Chemistry and Technologies for Energy
ICMATE-CNR
Corso Stati Uniti, 4, Padova 35127, Italy

M. Bonchio
Department of Chemical Sciences
University of Padova
Via Francesco Marzolo, 1, Padova 35131, Italy

M. Prato
Basque Foundation for Science (IKERBASQUE)
Plaza Euskadi, 5, Bilbao 48013, Spain

in aqueous media,[4] which are the most appealing for industrial application due to their cost benefits and low environmental impact.[5] Hence, the selective, efficient, cost-effective, and stable conversion of carbon dioxide into useful chemicals represents one of the key modern challenges in electrocatalysis.[6] The range of possible products is rather wide, with liquid products being especially attractive due to their high energy density, ease of storage, and wide industrial applications. Each product is formed through a specific multi-step pathway involving a number of electron and proton transfers, with each step subtending to a characteristic electric overpotential. Two key products that involve the transfer of 2 electrons are formic acid (HCOOH) and carbon monoxide (CO).[7,8]

Non-noble metal oxides (MO_x) are particularly interesting catalysts for CO_2RR due to their cost-effectiveness, their ability to favour CO_2 adsorption, and influence on product distribution. At a mechanistic level, MO_x are advantageous because they allow a simpler modulation of the local pH, and a more facile product desorption. Moreover, in many MO_x the tuning of the redox sites and oxygen vacancies within the structure is relatively facile, enabling control over the local environment of the reaction site. Among the various metal oxides, cerium oxide (CeO_2) stands out as a highly versatile material, whose structure and redox behaviour can be controlled and readily exploited.[9] However, bare CeO_2 nanoparticles lack in electronic conductivity and tend to aggregate, resulting in poor electrocatalytic effectiveness. Carbon phases can be used to improve such deficiencies,[10] and they are particularly useful if they possess controlled porosity and surface area.[11] Carbon Nanohorns (CNHs) can serve as an ideal support to alleviate such issues, as they present a high surface area and mesoporous texture which are beneficial for diffusion of the reagents, an electronic conductive network that facilitates electron transfer, and a stable framework that prevents aggregation of the supported nanoparticles.[12] This combination of properties allows to maximize the number of active sites, enhancing catalytic stability, and improving overall performance, making the CeO_2 supported on oxidized carbon nanohorns (CeO_2@oxCNHs) a highly promising material for CO_2RR applications.[7–13] In previous studies, we demonstrated the high activity of non-noble metal-based electrocatalysts when combined with carbon nanostructures.[14–17] In this work, we set to understand the structure-dependent electrochemical CO_2RR activity of CeO_2@oxCNHs by varying the catalyst synthetic approach. Specifically, we developed a solvothermal protocol that led to the deposition of small CeO_2 nanoparticles (ca. 5 nm) on oxCNHs. This nanocomposite catalyst could achieve one order of magnitude higher current density (*j*) than the corresponding CeO_2@oxCNHs material prepared by a previously reported sol-gel approach.[16,17]

P. Fornasiero
ICCOM-CNR URT Trieste
Via Licio Giorgieri, 1, Trieste 34127, Italy
M. Marchi
VSB - Technical University of Ostrava, Centre for Energy and Environmental Technologies
Nanotechnology Centre
17. listopadu 2172/15, Ostrava 70800, Czech Republic

Another essential aspect to be considered to boost the catalyst performances regards the supply of CO_2 to the electrode surface.[18–20] The Gas Diffusion Electrode (GDE) systems are innovatively designed to reverse the mode of CO_2 delivery to the catalyst surface. This design improves the interaction between the reactant and the catalyst, redefining the CO_2RR products spectrum.[21] The integration of GDEs with nanostructured porous materials enhances the three-phase interface, improving CO_2 distribution across the catalyst surface and boosting overall reaction efficiency. Hence, in the present work we also assessed and compared the catalyst's performance in both H-type cell and a GDE flow configuration.[8–10] This investigation provides valuable insights into the dependence of the reaction mechanisms on electrochemical cell configuration and the consequent switch of product selectivity.

Notably, we achieved a high selectivity toward liquid products, in particular formic acid (FE = 95% at −0.5 V vs RHE) in H-Type Cell and methanol (FE = 16% at −0.6 V vs RHE) in the Gas Diffusion Electrode configuration. This work underscores the critical role of both material innovation and device optimization in advancing CO_2RR technology.

2. Results and Discussion

The selected C-metal oxide nanohybrid (CeO_2@oxCNHs) was prepared by a sequence consisting of three steps, during which the CNHs were first oxidized by HNO_3 treatment. The oxidation step serves to attach oxygenated functionalities such as carboxylic acids or hydroxyls on the CNHs surface, in order to facilitate the binding of the metal centres.[22] Moreover, this treatment further enhance the surface area of the CNHs, as measured by N_2 physisorption analysis that passes from 438 to 612 $m^2\ g^{-1}$. Notably such surface areas are considerably higher than those of multi-walled carbon nanotubes (MWCNTs), which is 142 $m^2\ g^{-1}$ and that were previously used by us as the scaffold for layering metal oxides (Figure S7, Supporting Information). The oxidation was followed by a solvothermal method (S) that led to the formation of CeO_2 NPs directly on the oxidized CNHs (oxCNHs). This second step was aided by the presence of urea, which functioned as both the capping agent and contributed to the anchoring of the NPs to the carbon surface (**Figure 1**). Finally, a calcination step allowed for crystallization of the Ce oxide together with removal of the oxygenated functional groups on the CNHs. This synthetic strategy allowed for a better dispersion of the metal oxide nanoparticles as well as for an improved control of the particle size, which ranges from 2 to 8 nm (Figure S1C, Supporting Information). In contrast, the synthetic strategy previously used by our group for nanocarbon/ceria hybrids, which was based on sol-gel methods (G), resulted in CeO_2 nanoparticles large aggregates with a less homogeneous dispersion on the carbon support, as observed by TEM inspection (Figure 1D). However, more in depth nanoparticles morphology details emerged by a proper analysis at higher magnifications of regions of the samples with less concentrated nanoparticle distribution with round and oval shapes (Figure S1, Supporting Information). In particular, using the sol-gel method, slightly larger nanoparticle size distribution was calculated, ranging from 2 to 11 nm (Figure S1D, Supporting Information), with respect to the solvothermal method (Figure S1C, Supporting Information), which however could significantly affect the

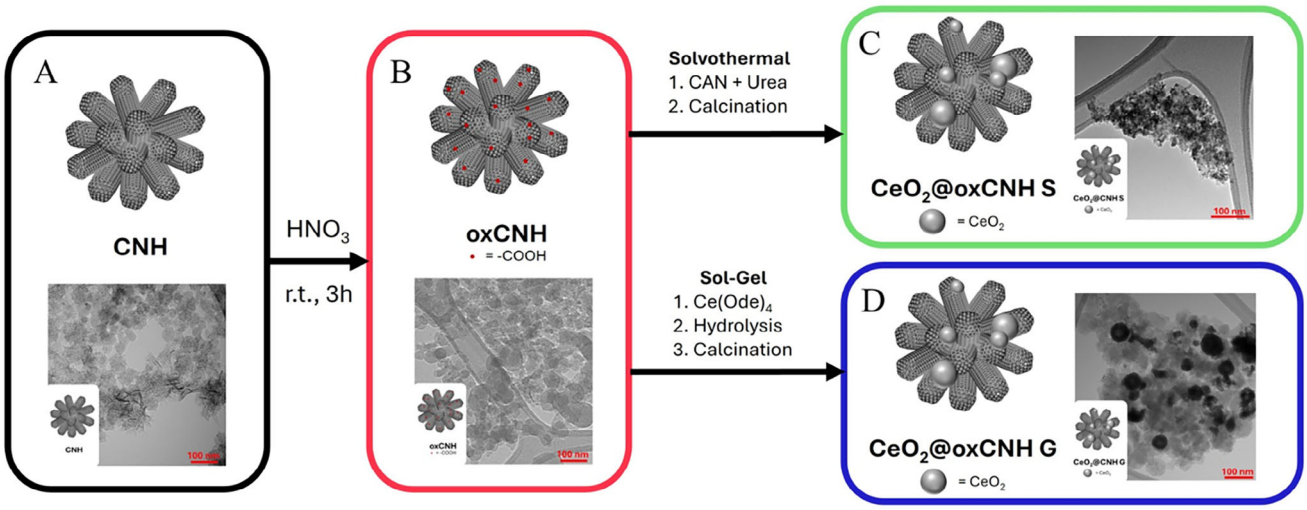

Figure 1. Schematic synthesis of CeO_2@oxCNHs nanocomposites: pristine CNHs A) are oxidized to oxCNHs B), which are then processed through Solvothermal (CeO_2@oxCNH-S, panel C) or Sol-Gel (CeO_2@oxCNH-G, panel D), followed by calcination, to attach CeO_2 nanoparticles. TEM images of the different synthesis and functionalization stages of CNHs with CeO_2 nanoparticles are reported in each panel. (CAN = Cerium Ammonium Nitrate; $Ce(ODe)_4$ = Cerium tetrakis(decyloxide)).

interfacial area between carbon and ceria. It is worth noting that the oxidation step on the pristine CNHs does not cause any significant damage on the structure, as confirmed by TEM images (Figure 1A-B).

The CeO_2 loading also differs for the two materials, as measured by thermogravimetric analysis (TGA). In particular, the solvothermal method secures a higher metal oxide loading (39 wt.%) than the sol-gel method (18 wt.%), (**Figure 2**A). While not producing visible change of morphology of the CNHs structure, the introduction of CeO_2 NPs seems to affect somehow the graphitic framework, as noted by the increased D/G band intensity ratio in the Raman spectra (Figure 2B) as compared to oxCNHs. For both CeO_2@oxCNH-S and CeO_2@oxCNH-G, Raman spectroscopy also confirms the presence of crystalline CeO_2, with the appearance of the characteristic ceria peak at ≈470 cm^{-1}.[16,23]

The two compounds were further characterized using X-ray Photoelectron Spectroscopy (XPS), and X-ray Diffraction (XRD) (**Figure 3**; Figures S4,S5 and S6, Supporting Information). The formation of CeO_2 nanoparticles was further confirmed by X-ray diffraction analysis (XRD), which shows the characteristic reflections of the CeO_2 cubic structure (see Figure S6, Supporting Information).[24,25] X-ray photoelectron spectroscopy (XPS) shows the successful introduction of oxygenated functional groups on the CNHs (critical for better anchoring of the Ce precursors), indicated by a significant enhancement of the O 1*s* signal in oxCNHs (Figure S3A, Supporting Information) with respect to C 1*s* if compared to pristine CNHs (Figure S2A, Supporting Information). The O 1*s* high-resolution XPS spectrum of the oxCNHs (Figure S3C, Supporting Information), if compared to pristine CNHs (Figure S2C, Supporting Information), shows a more complex chemical environment for oxygen with two components related to C-O single and double bonds, confirming the higher degree of oxygen functional groups. The cerium element in the CeO_2@oxCNH-S nanohybrid is present in mixed oxidation

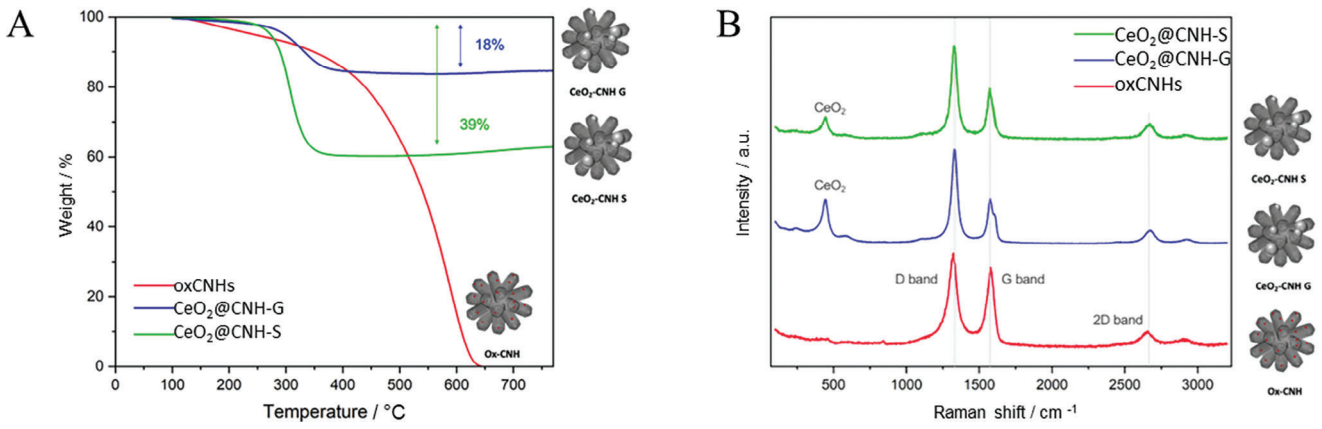

Figure 2. Thermogravimetric analysis (TGA) and Raman spectroscopy of CeO_2@oxCNHs obtained via solvothermal (S) and sol-gel (G) methods. A) TGA profiles for the solvothermal (green line) and the sol-gel (blue line) methods compared to oxCNHs without CeO_2 (red line). B) Raman spectra of CeO_2@oxCNH-S (green line), CeO_2@oxCNH-G (blue line), and oxCNHs (red line).

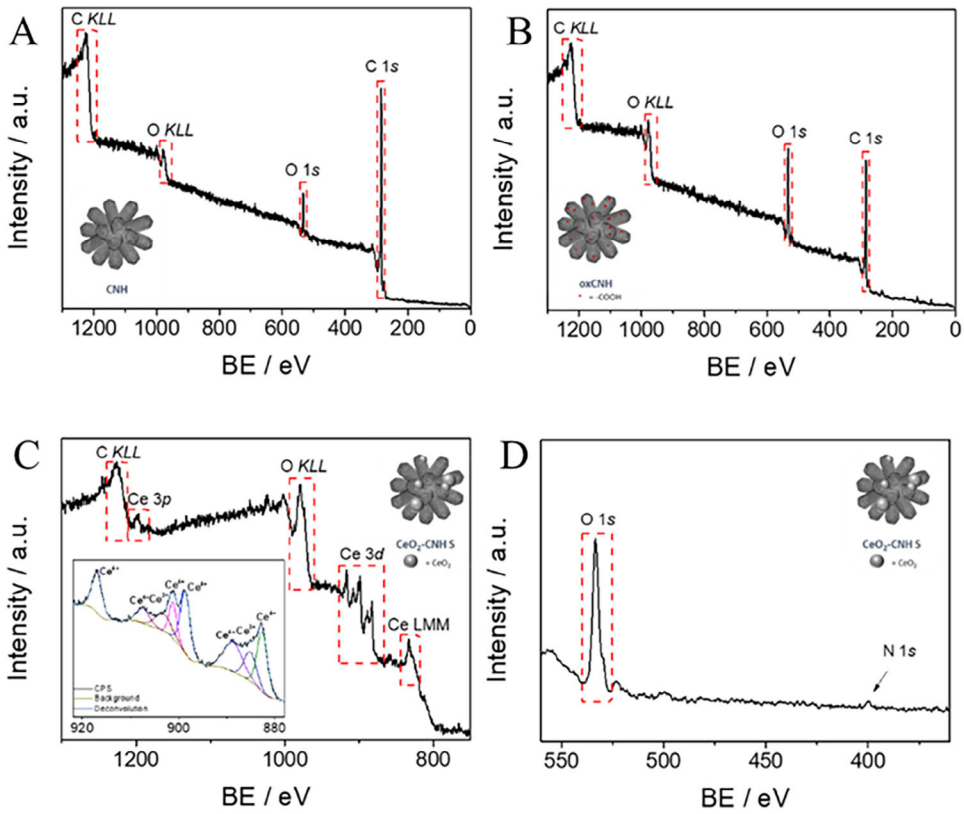

Figure 3. XPS of CeO_2@oxCNH-S compared with data from pristine CNHs and oxCNHs. A) Survey XPS spectrum of pristine CNHs; B) Survey XPS spectrum of oxCNHs, C) Survey XPS spectrum of CeO_2@oxCNH-S at high binding energy. The inset picture in C shows the deconvolution of XPS signal of the Ce 3d orbital. D) XPS of CeO_2@oxCNH-S at low binding energy, showing the peaks of the O 1s and N 1s.

states III and IV, as noted by the deconvolution of the 3*d* levels in the high-resolution spectra (Figure S4A,D and Table S1, Supporting Information).[17] It should be noted that in the O 1*s* high-resolution spectrum, the component at 529.7 eV is indicative of the O-Ce bonds (Figure S4C, Supporting Information).[26] Finally, a slow intensity peak of N 1*s* suggests the incorporation of minor levels of nitrogen, presumably from urea (Figure 3D). Perhaps due to its lower metal oxide content, XPS of CeO_2@oxCNHs-G showed lower and broader signals for the Ce (Figure S5, Supporting Information). A low intensity signal of Ce LMM (Figure S5A, Supporting Information) is symptomatic of lower loading of Ce in the material, according also to the TGA results (Figure 2A) and confirmed by the appearing of the Ce $4p_{1/2}$ orbital in the 220–240 eV range (Figure S5D, Supporting Information).[26]

2.1. Synergistic Effect of CO_2RR

Cyclic voltammetry (CV) in 0.5 M $KHCO_3$ (Ar-saturated) revealed distinct electrochemical behaviours for the two different catalysts CeO_2@oxCNH-S and CeO_2@oxCNH-G (**Figure** 4A green and blue respectively and Figure S8, Supporting Information). The sol-gel sample exhibited a capacitive current with a CeO_2 redox peak weakly pronounced, suggesting a dominant non-faradaic behaviour due to the greater exposure of the CNHs surface (Figure 4A; Figure S8B, Supporting Information). In contrast, the solvothermal catalyst exhibited a *j* twenty times higher than its sol-gel counterpart and displayed distinct Ce redox fingerprint peaks (Figure 4A; Figure S8A, Supporting Information). At $E_{\frac{1}{2}} = 1.10\ V\ vs\ RHE$ the reversible conversion between Ce^{4+} and Ce^{3+} was observed (Equation 1).[14,27]

$$2\,CeO_{2\,(surface)} + 2\,e^- + 2\,H^+ \rightleftarrows Ce_2O_{3\,(surface)} + H_2O \quad (1)$$

Notably, the nanomaterial interface promotes the reduction of CeO_2, leading to an increase in Ce^{3+} content, as evidenced by the purely capacitive behaviour observed in the CV profiles of CeO_2 (black) and oxCNH (red).

The electrocatalytic properties of the better-performing CeO_2@oxCNH-S were further assessed by means of chronoamperometry measured in a custom-built H-type cell operating in static mode. This configuration, without forcing the mass transport, allows for a more accurate assessment of intrinsic material properties. In this setup, positioning the working electrode facing upward ensures the most efficient transfer of gaseous products to the Gas Chromatograph, minimizing losses.[15] The Glassy Carbon Electrode (GCE) and Chronoamperometry (CA) performed for 1 h and 51 min at different fixed potential ranging from −0.5 to −0.9 V vs RHE.

Gas-phase products were analysed in-line using Gas Chromatography (GC), while liquid-phase products were analysed post-experiment using Ionic Chromatography (IC) and Nuclear

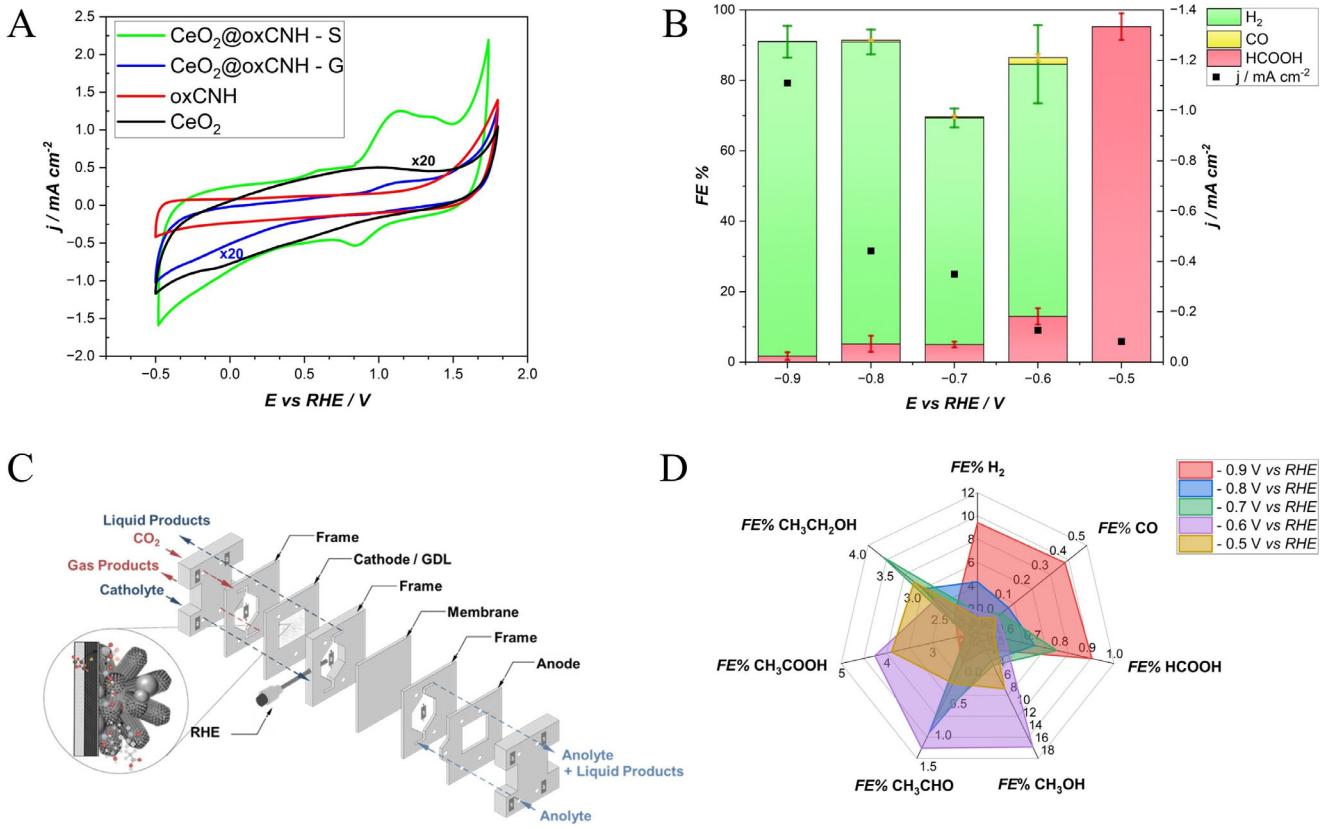

Figure 4. Performances of the CeO_2@oxCNH. A) Cyclic Voltammetry (CV) of CeO_2@oxCNH-S (in green),CeO_2@oxCNH-G (in blue), CeO_2 (in black), and oxCNHs (in red) mantaining the CeO_2 and the oxCNHs amount fixed in Ar-saturated 0.5 M $KHCO_3$ electrolyte at 20 mV s^{-1}. B) CO_2RR Performance in a H-Type Cell. Left axis: FE% of detectable CO_2RR products in CO_2-saturated $KHCO_3$ 0.5 M (pH 7.5): H_2 (green), CO (yellow), HCOOH (red). Right axis: Current density at the corresponding potential, represented by black squares. C) Scheme of Functioning of a three-electrode Flow Cell Device with a focus of Gas Diffusion Layer coated with CeO_2@oxCNH. D) Radar plot of FE% of CO_2RR performance in a Flow Cell in $KHCO_3$ 0.5 M in the −0.5 −0.9 V versus RHE range. The detected products include H_2, CO, HCOOH, CH_3OH, CH_3CHO, CH_3COOH, and CH_3CH_2OH. Statistical results are based on three independent replicates ($n = 3$), with error bars representing standard deviations.

Magnetic Resonance (^{1}H NMR) Spectroscopy. Faradaic efficiency (FE) was calculated as described in the Supporting Information (Equations S1 and S2, Supporting Information).[14,17,28,29] In this H-type cell, hydrogen (H_2) was the dominant product across most of the tested potentials (Figure 4B). However, it is worth remarking that at −0.5 V vs RHE, formic acid (FA) production was significantly enhanced, achieving a Faradaic Efficiency (FE) of 95%, effectively suppressing the competing hydrogen evolution reaction (HER). Carbon monoxide (CO) was also detected but with low efficiency at all potentials. This low CO production aligns with the known behaviour of CeO_2 surfaces, which preferentially stabilize the *OCHO intermediate over CO formation.[2] This behaviour is attributed to the non-stoichiometric nature of CeO_2 and the presence of oxygen vacancies formed during electrolysis. These vacancies, which become more prevalent as the nanomaterial size decreases, are stabilized by the oxCNHs nanostructure. The resulting oxygen deficiency increases the concentration of Ce^{3+} in the catalyst, promoting the stabilization of oxygen-bound intermediates and favouring formic acid production. Inspired by previous studies on CO_2RR catalysed by Pd nanoparticles,[31,32] we had previously hypothesized that in MWCNT@CeO_2 systems under moderate electric potential, the Ce^{3+} centres are possibly present in the form of Ce hydride species. These Ce-H species can open a direct electrohydrogenation pathway which explains the very small overpotential required for FA generation.[17,33] Notably, while the previous MWCNT@CeO_2 could achieve a maximum FE of 65% for FA, the new assembly design based on CNHs allow for a 95% FE (Figure 4B).

Based on these results, the CO_2 reduction capability of CeO_2@oxCNH-S was examined in more detail using a flow setup with a GDE (Figure 4C). In the GDE system, the CO_2 is supplied from the back of the electrode, instead of approaching the front face as in H-type cell systems, ensuring optimal distribution across the catalyst layer. The main difference stems from variations in mass transport between the two systems: in H-type setups, the amount of CO_2 that can be converted into valuable products is limited by its solubility threshold in aqueous media.[34] GDE systems, with their inherent complexity, can lead to a different range of CO_2RR products, directly converting the CO_2.[21,34] As a result, GDEs are widely employed to drive the reaction toward liquid products, which often involve sluggish kinetics and require C—C coupling.[35] The use of nanostructured materials, such as the CeO_2@oxCNHs proposed in this work, enables a

uniform and efficient distribution of CO_2 across the entire catalytic surface, giving the possibility to form a C—C bond.

In addition, the nanostructured nature of the materials ensures optimal ionomer distribution, which minimizes GDE flooding by increasing the hydrophobicity of the catalyst layer.[36]

As expected, flow cell configuration results in higher current density (*j*) (one order of magnitude higher than in the H-type) and expands the range of CO_2RR products on the CeO_2@oxCNHs surface. At −0.8 V vs RHE the *j* reaches the significant value of −4.7 mA cm^{-2} (see Figure S11, Supporting Information), and an enhancement in *j* is observed throughout the explored potential range at all the potential explored. Indeed, this trend is mirrored by an increased number of products detected. The hydrogen production is significantly suppressed, as expected using a high-thickness gas diffusion electrode (For further details, see Supporting Information, CO_2RR catalytic performance of the solvothermal sample).[37]

The detected molecules are cascade products, with a preference for liquid products, particularly alcohols such as methanol and ethanol,[38] while the HER never exceeds 10% FE. Among the CO_2RR products, methanol is the most favoured, appearing at all explored potentials. Its concentration peaks at the less negative potential (17 ppm at −0.6 V vs RHE), where CO is absent. In contrast, CO becomes the dominant product as the applied potential becomes more negative, reaching 30 ppm at −0.9 V v RHE. This result is significant because CO and methanol are competing C_1 products, both requiring a carbon-intermediate bond. The mechanism involved follows the lowest-energy pathway.[4,39–41] The FA, among the C_1 products, is the minor one, and shows a linear increase with the applied potential (Figure 4D). The products analysis reveals a strong dependence of product distribution on the applied potential, with more highly reduced products (e.g., CH_3OH and CH_3CHO) favoured at less negative potentials. Those findings are particularly interesting because are in contrast with the known behaviour of the ceria to drive the reaction in the formic acid direction thanks to the oxygen vacancies.

The preference for *COOH intermediates over *OCHO ones is also evident in the analysis of C_2 products. Their formation is facilitated by carbon coordination on the catalyst surface, aligning with the preferential production of CH_3OH and CO as C_1 products. Ethanol concentration remains constant across the explored potential range, while its competing product, acetaldehyde, appears only when CO is absent.

It is important to highlight that catalyst selectivity is optimal when CO_2 and *CO concentrations are balanced and that C_2 product formation correlates with increased *CO concentration, which promotes $*CH_2CHO$ intermediate and leads to acetaldehyde and ethanol production, both desirable products. These follow a similar reaction pathway, beginning with *CO dimerization. However, at excessively high *CO coverage, the reaction shifts undesirably toward acetate formation rather than ethanol. This suggests that the predominant presence of acetate in the absence of CO is not an indication of improved selectivity but rather a side effect of excessive *CO accumulation on the catalyst's surface.[42,43] An alternative hypothesis suggests that acetate may also originate from the disproportionation of acetaldehyde.[39]

Product analysis reveals that the product range is influenced by flux, which shifts preferential coordination from *OCHO intermediates to *COOH. The role of flux is to increase the concentration of CO_2 at the catalyst surface, enhancing the probability of C—C coupling that is a known behaviour on cerium oxide catalysts.[44] This effect correlates with increased current density at the electrode surface, emphasizing the improved catalytic activity and selectivity driven by a continuous CO_2 supply. Consequently, CO_2 delivery plays a crucial role in shaping product distribution and efficiency during CO_2RR.[36,42,45] The transition from FA to C_1 products beyond CO suggests a shift in the stabilization of key intermediates, potentially driven by increased surface coverage of *CO, which can be enhanced by raising local CO_2 concentration. Lastly, the long-term durability of the catalyst was assessed under continuous operation. Notably, the GDE system remained stable during 24 h of continuous CA, consistently producing formic acid throughout the experiment, with its concentration increasing linearly over time (see Figure S10, Supporting Information).

3. Conclusion

This study demonstrates that oxCNHs combined with CeO_2 enhance performance in the electrochemical reduction of CO_2 (CO_2RR). The choice of synthesis method influences the properties of CeO_2@oxCNHs, with the solvothermal method (S) outperforming the sol-gel method (G) by yielding smaller, more homogeneously dispersed CeO_2 nanoparticles, higher metal oxide loading (39 wt% vs 18 wt%), and better integration with the carbon scaffold. These improvements result in enhanced electrocatalytic performance, evidenced by higher current densities.

Electrocatalytic tests revealed that in a H-type static system, a high Faradaic efficiency (95%) for formic acid was achieved at −0.5 V vs RHE. Implementing a flow system with a Gas Diffusion Electrode (GDE) significantly increased current density and expanded the product range, enabling the formation of alcohols (methanol and ethanol) and other C_2 products. A key finding is the shift in the preferred intermediate: while oxygenated intermediates dominate in an H-type cell due to the oxygen vacancies of the material, the GDE system's performance is primarily driven by the CO_2 flux. This change in product distribution is closely linked to the CO_2 delivery method, emphasizing the critical role of local CO_2 concentration in determining catalytic selectivity.

Furthermore, the results reveal that the formation of C_2 products is driven by *CO concentration, which promotes C—C coupling and favours acetaldehyde and ethanol production. However, excessive *CO coverage leads to an undesired shift toward acetate formation. These findings highlight the importance of optimizing both CO_2 flux and *CO coverage to improve product selectivity. The long-term stability of the GDE system further demonstrates its potential for practical, sustained CO_2RR applications.

4. Experimental Section

Synthesis and Characterization of CeO_2@oxCNHs: CNHs (250 mg purchased from Carbonium) were first oxidized (oxCNHs) with diluted HNO_3 (250 mL, 4 M) at room temperature for 3 h and purified by a sequence of: i. microfiltration (0.1 µm PTFE filters), ii. washing (steps in succession using water, DMF, and ethanol), iii. Drying at 80 °C overnight obtaining 243 mg of fine powder.[30] The as prepared oxCNHs (10 mg) were suspended in an

ethylene glycol (25 mL) solution of Ammonium Cerium (IV) Nitrate (CAN, 32 mg) and urea (17.5 mg). This mixture was heated at 200 °C for 48 h under atmospheric pressure in an open reactor flask equipped with a reflux condenser. The solid was washed by centrifugation with water, methanol, and ethanol and finally recovered by microfiltration under vacuo (0.1 µm PTFE filters), dried at 80 °C overnight, and finally subjected to calcination in air at 250 °C for 5 h (Figure 1C).

For comparison, the synthesis was also carried out using a previously reported approach by our group, based on sol-gel methods.[17] oxCNHs (20 mg) were suspended in ethanol (2 mg mL^{-1}) and a 0.25 M Ce(IV) tetrakis(decyloxide) THF solution (1.37 mL) was added dropwise under sonication at room temperature. Then, a water/THF 1/10 solution (11 mL) slowly dropped to the resulting mixture under continuous sonication. The obtained product was separated as powder by microfiltration (0.1 µm PTFE filters) and subjected to several washings with THF. The solid was finally dried at 80 °C overnight and calcined in air at 250 °C for 5 h (Figure 1D).

Physical Characterization Methods: X-ray diffraction analysis was performed using a Malvern PANalytical Empyrean diffractometer, equipped with a sealed Co Kα tube, with an Fe β-filter, and 1Der sold-state detector. Data were collected over a 2θ range of 5–100° with a step size of 0.021°. TEM measurements were performed on a TEM Philips EM208, using an acceleration voltage of 100 kV. Samples were prepared by drop casting the dispersed particles onto a TEM grid (200 mesh, copper, carbon only). Raman spectra were recorded on a inVia Renishaw microspectrometer equipped with a Nd:YAG laser using an excitation wavelength of 532 nm. Preparation of the samples was carried out via drop casting the dispersed particles onto silicon wafers, which were then analysed. For each sample, 5 points were recorded and averaged. Thermogravimetric analysis (TGA) was carried out on a TA Discovery TGA 550 instrument with heating rate of 10 °C min^{-1} under air flow. N_2 physisorption at the liquid nitrogen temperature was collected using a Micromeritics ASAP 2020 analyser. Before analysis, the samples were degassed at 150 °C for at least 12 h at a pressure lower than 10 µmHg. The specific surface area of the samples was calculated applying the BET method.

Electrochemical Measurements: The material was further characterized by electrochemical techniques to understand the CO_2RR performances. The two CeO_2@oxCNHs batch synthesized trough solvothermal method and sol gel method, were evaluated by Potentiostatic Electrochemical Impedance (PEIS) and Cyclic Voltammetry (CV). Chronoamperometry (CA) was used to understand the performances in CO_2 conversion of the solvothermal sample. The measures were conducted in three electrodes devices, using 0.5 M$KHCO_3$ solution pre-electrolyzed before each experiment. All the solutions were thoroughly degassed with CO_2 for 30 min before each experiment. The CO_2RR products were analysed by online gas chromatography (GC), while the liquid phase trough Ion Chromatography (IC) or Nuclear Magnetic Resonance (NMR) spectroscopy. The electrodes were prepared for drop casting technique, after solubilized the solid catalysts in an Isopropyl Alcohol/Water/Nafion mixture (1.6 mg mL^{-1}). To determine the optimal loading for the GDE, three different loadings were tested: 200, 500, and 1000 µg cm^{-2} (see Figure S9, Supporting Information). The highest Faradaic Efficiency (FE%) was achieved at 200 µg cm^{-2}, while the highest current density ($j = 4.6$ mA cm^{-2}) was observed at 500 µg cm^{-2}. To maintain consistency with the Glassy Carbon Electrode coating and align with this previous studies, the 500 µg cm^{-2} loading was selected for further investigation on the GDE.[14,17] The coverage film was obtained with aliquots defined in base of the substrate (GC 0.071 cm^2, GC 1 cm^2, and GDE39BB 1 cm^2) (see the Supporting Information for details, **Electrochemistry**).

The 1 cm^2 Working Electrodes (Glassy Carbon Electrode GCE or GDE) were coated with a CeO_2@oxCNHs nanofilm via drop casting. In the presented configuration, this systems allow for precise quantification of products, owing to the reduced catholyte volume (CO_2 saturated $KHCO_3$ 0.5 M) and direct gas delivery to the gas chromatograph.[46] The liquid phase was detected using Ionic Chromatography (IC) or Nuclear Magnetic Resonance (^{1}H NMR) Spectroscopy. The IC was used to detect formic acid and acetate, while ^{1}H NMR spectroscopy was used to identify and quantify methanol, ethanol, and acetaldehyde in the liquid phase. The NMR analysis used 0.4 mM dimethyl sulfoxide (DMSO) as an internal standard, with a mixture of 500 µL of the liquid sample with 100 µL of deuterium oxide (D_2O) for accurate measurement.[47–49]

Supporting Information

Supporting Information is available from the Wiley Online Library or from the author.

Acknowledgements

A.P. and M.C. contributed equally to this work. This research was funded by the European Commission (H2020 – RIA-CE-NMBP-25 Program, Grant No. 862 030, project DECADE), by Italian MUR, project NANOARC: Bio-inspired PhotoElectroCatalytic NanoArchitectures for Energy Conversion and Storage, grant number 20228YFRNL, CUP J53D23008600006 and by MASE – Next Generation EU, project PRIDE (RSH2A_000037), and Next Generation EU, project ECHO-EF grant number P2022WANKS_002, CUP J53D23014620001. We acknowledge "ECOSISTER" funded under the National Recovery and Resilience Plan (NRRP), Mission 04 Component 2 Investment 1.5 – NextGenerationEU (Call for tender n. 3277, 30/12/2021; Award Number 0 001052, dated 23/06/2022). We acknowledge financial support from the European Union under the REFRESH Research Excellence For REgion Sustainability and High tech Industries project number CZ.10.03.01/00/22_003/0000048 via the Operational Programme Just Transition.

Conflict of Interest

The authors declare no conflict of interest.

Data Availability Statement

The data that support the findings of this study are available from the corresponding author upon reasonable request.

Keywords

carbon nanohorns, ceria, CO_2 reduction reaction, electrochemistry, nanomaterial

Received: April 13, 2025
Revised: July 9, 2025
Published online:

[1] F. Rotondo, P. Perchinunno, S. L'Abbate, L. Mongelli, *Sci. Rep.* **2022**, *12*, 18513.
[2] T. K. Todorova, M. W. Schreiber, M. Fontecave, *ACS Catal.* **2020**, *10*, 1754.
[3] Y. J. Zhang, V. Sethuraman, R. Michalsky, A. Peterson, *ACS Catalysis* **2014**, *4*, 3742
[4] A. Rendón-Calle, S. Builes, F. Calle-Vallejo, *Curr. Opin. Electrochem.* **2018**, *9*, 158.
[5] X. Zhang, S. X. Guo, K. A. Gandionco, A. M. Bond, J. Zhang, *Mater. Today Adv.* **2020**, *7*, 100074.
[6] M. T. M. Koper, *J. Electroanal. Chem.* **2011**, *660*, 254.
[7] Y. Kuang, H. Rabiee, L. Ge, T. E. Rufford, Z. Yuan, J. Bell, H. Wang, *Energy and Environmental Materials* **2023**, *6*, 12596.
[8] M. Moro, G. Tuci, A. Rossin, C. Salvatici, E. Verlato, C. Evangelisti, F. Paolucci, G. Valenti, Y. Liu, G. Giambastiani, *ACS Mater. Lett.* **2024**, *6*, 583.

[9] T. Montini, M. Melchionna, M. Monai, P. Fornasiero, *Chem. Rev.* **2016**, *116*, 5987.
[10] H. A. Miller, A. Lavacchi, F. Vizza, M. Marelli, F. Di Benedetto, F. D'Acapito, Y. Paska, M. Page, D. R. Dekel, *Angew. Chem., Int. Ed.* **2016**, *55*, 6004.
[11] J. Ying, G. Jiang, Z. Paul Cano, L. Han, X. Y. Yang, Z. Chen, *Nano Energy* **2017**, *40*, 88.
[12] S. Zhu, G. Xu, *Nanoscale* **2012**, *2*, 2538.
[13] E. Verlato, N. Comisso, L. Mattarozzi, M. Musiani, L. Vázquez-Gómez, *Electrochim. Acta* **2024**, *492*, 144344.
[14] M. Melchionna, M. Moro, S. Adorinni, L. Nasi, S. Colussi, L. Poggini, S. Marchesan, G. Valenti, F. Paolucci, M. Prato, P. Fornasiero, *ACS Appl. Energy Mater.* **2022**, *5*, 13356.
[15] M. Liu, F. Hof, M. Moro, G. Valenti, F. Paolucci, A. Pénicaud, *Nanoscale* **2020**, *12*, 20165.
[16] M. V. Bracamonte, M. Melchionna, A. Giuliani, L. Nasi, C. Tavagnacco, M. Prato, P. Fornasiero, *Sens. Actuators, B* **2017**, *239*, 923.
[17] G. Valenti, M. Melchionna, T. Montini, A. Boni, L. Nasi, E. Fonda, A. Criado, A. Zitolo, S. Voci, G. Bertoni, M. Bonchio, P. Fornasiero, F. Paolucci, M. Prato, *ACS Appl. Energy Mater.* **2020**, *3*, 8509.
[18] M. de Jesus Gálvez-Vázquez, P. Moreno-García, H. Xu, Y. Hou, H. Hu, I. Z. Montiel, A. V. Rudnev, S. Alinejad, V. Grozovski, B. J. Wiley, M. Arenz, P. Broekmann, *ACS Catal.* **2020**, *10*, 13096.
[19] W. Choi, Y. Chae, E. Liu, D. Kim, W. S. Drisdell, H.-S. Oh, J. H. Koh, D. K Lee, U. Lee, D. H Won, *Nat. Commun.* **2024**, *15*, 8345.
[20] C. Ampelli, F. Tavella, D. Giusi, A. M. Ronsisvalle, S. Perathoner, G. Centi, *Catal. Today* **2023**, *421*, 114217.
[21] T. Möller, T. Ngo Thanh, X. Wang, W. Ju, Z. Jovanov, P. Strasser, *Energy and Environmental Science* **2021**, *14*, 5995.
[22] M. Melchionna, M. Prato, *ECS J. Solid State Sci. Technol.* **2013**, *2*, M3040.
[23] J. E. Spanier, R. D. Robinson, F. Zhang, S.-W. Chan, I. P. Herman, *Phys. Rev. B* **2001**, *64*, 245407.
[24] A. Beltram, M. Melchionna, T. Montini, L. Nasi, R. J. Grote, M. Prato, P. Fornasiero, *Catal. Today* **2015**, *253*, 142.
[25] J. Qian, Z. Chen, H. Sun, F. Chen, X. Xu, Z. Wu, P. Li, W. Ge, *ACS Sustainable Chem. Eng.* **2018**, *6*, 9691.
[26] A. Pereira, M. Blouin, A. Pillonnet, D. Guay, *Mater. Res. Express* **2014**, *1*, 015704.
[27] C. Y. Cummings, S. J. Stott, M. J. Bonné, K. J. Edler, P. M. King, R. J. Mortimer, F. Marken, *Journal of Solid-State Electrochemistry* **2008**, *12*, 1541.
[28] Q. Lu, F. Jiao, *Nano Energy* **2016**, *29*, 439.
[29] N. Dutta, D. Bagchi, G. Chawla, S. C. Peter, *ACS Energy Lett.* **2024**, *9*, 323.
[30] D. Ješić, D. Lašič Jurković, A. Pohar, L. Suhadolnik, B. Likozar, *Chem. Eng. J.* **2021**, *407*, 126799.
[31] X. Min, M. W. Kanan, *J. Am. Chem. Soc.* **2015**, *137*, 4701.
[32] M. Melchionna, M. V. Bracamonte, A. Giuliani, L. Nasi, C. Tavagnacco, M. Bonchio, P. Fornasiero, M. Prato, *Energy, Environmental Science* **2018**, *11*, 1571.
[33] Z. Wu, Y. Cheng, F. Tao, L. Daemen, G. S. Foo, L. Nguyen, X. Zhang, A. Beste, A. J. Ramirez-Cuesta, *J. Am. Chem. Soc.* **2017**, *139*, 9721.
[34] T. Burdyny, W. A. Smith, *Energy and Environmental Science* **2019**, *12*, 1442.
[35] Q. Chen, X. Wang, Y. Zhou, Y. Tan, H. Li, J. Fu, M. Liu, *Adv. Mater.* **2024**, *36*, 2303902.
[36] T. Zhang, Z. Li, X. Lyu, J. Raj, G. Zhang, H. Kim, X. Wang, S. Chae, L. Lemen, V. N. Shanov, J. Wu, *J. Electrochem. Soc.* **2022**, *169*, 104506.
[37] N. T. Nesbitt, T. Burdyny, H. Simonson, D. Salvatore, D. Bohra, R. Kas, W. A. Smith, *ACS Catal.* **2020**, *10*, 14093.
[38] W. Zheng, X. Yang, Z. Li, B. Yang, Q. Zhang, L. Lei, Y. Hou, *Angew. Chem., Int. Ed.* **2023**, *62*, 2027.
[39] Y. Y. Birdja, E. Pérez-Gallent, M. C. Figueiredo, A. J. Göttle, F. Calle-Vallejo, M. T. M. Koper, *Nat. Energy* **2019**, *4*, 732.
[40] H. Li, Y. Li, M. T. M. Koper, F. Calle-Vallejo, *J. Am. Chem. Soc.* **2014**, *136*, 15694.
[41] X. Nie, M. R. Esopi, M. J. Janik, A. Asthagiri, *Angew. Chem., Int. Ed.* **2013**, *52*, 2459.
[42] L. Xu, P. Trogadas, M. O. Coppens, *Adv. Energy Mater.* **2023**, *13*, 2302974.
[43] F. Calle-Vallejo, M. T. M. Koper, *Angew. Chem., Int. Ed.* **2013**, *52*, 7423.
[44] D. Esrafilzadeh, A. Zavabeti, R. Jalili, P. Atkin, J. Choi, B. J. Carey, R. Brkljača, A. P. O'Mullane, M. D. Dickey, D. L. Officer, D. R. MacFarlane, T. Daeneke, K. Kalantar-Zadeh, *Nat. Commun.* **2019**, *10*, 865.
[45] A. Wagner, C. D. Sahm, E. Reisner, *Nat. Catal.* **2020**, *3*, 775.
[46] E. Verlato, S. Barison, Y. Einaga, S. Fasolin, M. Musiani, L. Nasi, K. Natsui, F. Paolucci, G. Valenti, *J. Mater. Chem. A* **2019**, *7*, 17896.
[47] N. R. Babij, E. O. McCusker, G. T. Whiteker, B. Canturk, N. Choy, L. C. Creemer, C. V. De Amicis, N. M. Hewlett, P. L. Johnson, J. A. Knobelsdorf, F. Li, B. A. Lorsbach, B. M. Nugent, S. J. Ryan, M. R. Smith, Q. Yang, *Organic Process Research and Development* **2016**, *20*, 661.
[48] H. P. Iglesias van Montfort, S. Subramanian, E. Irtem, M. Sassenburg, M. Li, J. Kok, J. Middelkoop, T. Burdyny, *ACS Energy Lett.* **2023**, *8*, 4156.
[49] T. Chatterjee, E. Boutin, M. Robert, *Dalton Trans.* **2020**, *49*, 4257.